



Numerical modeling of optical coherent transient processes with complex configurations—I. Angled beam geometry

Tiejun Chang^{a,*}, Mingzhen Tian^b, Wm. Randall Babbitt^{a,b}

^a*The Spectrum Laboratory, Montana State University, Bozeman, MT 59717, USA*

^b*Department of Physics, Montana State University, Bozeman, MT 59717, USA*

Abstract

We present a theoretical model for optical coherent transient (OCT) processes based on Maxwell–Bloch equations for angled beam geometry. This geometry is critical in various OCT applications where the desired coherence outputs need to be spatially separated from the rest of the field. The model takes into account both the local interactions between inhomogeneously broadened two-level atoms and the laser fields, and the field propagation in optically thick media. Under the small-angle condition, the spatial dimensions transversing to the main propagation direction were treated with spatial Fourier transform to make the numerical computations for the practical settings confined within a reasonable time frame. The simulations for analog correlators and continuous processing based on stimulated photon echo have been performed using the simulator developed using the theory.

© 2004 Elsevier B.V. All rights reserved.

PACS: 42.10; 42.10.M; 42.40

Keywords: Maxwell–Bloch equations; Optical coherent transient; Photon echo; Angled beam geometry

1. Introduction

Optical coherent transient (OCT) effects in an inhomogeneously broadened medium are the basis for the proposed ultra-high performance systems for optical storage and processors, such as analog correlators, optical routers, and true-time delays [1–5]. The fully coupled Maxwell–Bloch equations are required to adequately study the problem of the laser field propagation and the coherent transient processes, especially in the thick media [6,7]. The coherent effects of light interacting with an ensemble

of inhomogeneously broadened two-level atoms is governed by Bloch equations, where the electric field acts as a source to drive the atomic dipoles. The propagation effects of the field in a thick medium are governed by Maxwell equations, where the atomic dipoles act as a source of macroscopic polarization feedback to the electric field.

The coupled Maxwell–Bloch equation simulations used for studying OCT so far have dealt with the collinear configuration, where the electric field of the inputs and the induced signals including the free-induction decay, the optical nutation and the photon echoes were treated as plane wave propagating along one direction [6–8]. The non-dispersive condition was also assumed, where the macroscopic in-quadrature atomic polarization

*Corresponding author. Tel.: +1-406-994-7308; fax: +1-406-994-6767.

E-mail address: chang@spectrum.montana.edu (T. Chang).

summarized to zero [9,10]. The problem was solved by numerical integration in three dimensions along one spatial, a time and a frequency axes. However, in most OCT devices, the output echoes, which usually carry the processed signals, are required to be spatially separated from the inputs and other induced fields, such as the free-induction decay and higher order echo signals. This has been done in various experiments with angled beam configurations [5,11,12]. Usually, a box geometry is used to separate four beams involved in a stimulated photon echo (SPE) process, as shown in Fig. 1(a). The wave vector of the echo field, \vec{k}_e is determined by the wave vectors of three inputs $\vec{k}_1, \vec{k}_2, \vec{k}_3$ as $\vec{k}_e = \vec{k}_3 + \vec{k}_2 - \vec{k}_1$, according to the causality. In order to simulate the OCT processes using Maxwell–Bloch equations under this setting, two more spatial dimensions have to be included in the equations, which makes the equations too tedious for the numerical solution. The simulation for a practical setting is almost impossible within a reasonable time frame. Fortunately, one can simplify the model by tracking the plane waves in a few directions instead of solving for the field distribution in three-dimensional space, since all the input and echo pulses have very well-defined propagation directions. The directions that need to be tracked

can be selected according to the incident directions of the input pulses and the directions of echoes of interest. The spatial Fourier transform can be used to convert a 3-D field into a few plane wave pulses traveling in different directions. The model can be further simplified by ignoring the absorption length variation related to propagation direction when the angles between the beams are small.

In this paper, we first derive a set of generalized collinear Maxwell–Bloch equations with a slowly varying phase term in the electric field. This phase term, novel compared to the previous models, is critical for including the more complex figures in the pulses, such as, the frequency and/or phase modulations and/or the angled beam configurations. Then, the model will be developed for the angled beam configuration where the beams spatial directions were converted to the spatial phase terms using Fourier transform. Some simulation results for OCT correlator and SPE's from quasi-continuous probe fields will be discussed.

2. Theoretical model

2.1. Maxwell–Bloch equations with arbitrary phase modulation

The Maxwell–Bloch equations that treat the medium quantum mechanically and treat the field classically governing the evolution of the field and the atomic polarization and population components in an inhomogeneously broadened medium. The field is assumed propagating along the z -axis in space with the angular frequency ω_0 and the wave vector k , and the phase $\varphi(z, t)$ that is a function of time, t , and spatial coordinate z . The electric field in the medium can be written as

$$E(z, t) = \frac{\hbar}{\mu} \Omega(z, t) \cos[\omega_0 t - kz + \varphi(z, t)], \quad (1)$$

where $\Omega(z, t)$ is the slowly varying amplitude in Rabi frequency and μ denotes the dipole moment of the atomic transition. A slow varying phase term $\varphi(z, t)$ is generalized and can be the result of the frequency, phase and spatial phase modulations of the field. Usually, the field propagation

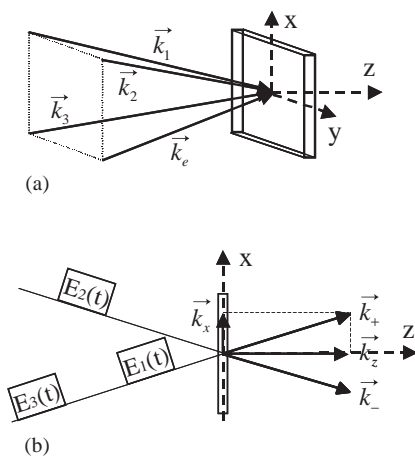


Fig. 1. (a) The box geometry with four beams whose directions are represented by the wave vectors $\vec{k}_1, \vec{k}_2, \vec{k}_3$ and \vec{k}_e . (b) The angled-beam scheme for OCT processes with two beams in directions \vec{k}_+ and \vec{k}_- .

equations contain the Rabi frequency $\Omega(z, t)$ and phase $\varphi(z, t)$ [13,14]. However, with these equations, the calculation finds it difficult to handle the case when the field amplitude approaches zero where the phase is undefined. We choose another pair of variables, in-phase Ω_c and in-quadrature Ω_s components of the field, defined as

$$E(z, t) = \frac{\hbar}{\mu} [\Omega_c(z, t) \cos(\omega_0 t - kz) + \Omega_s(z, t) \sin(\omega_0 t - kz)], \quad (2)$$

where

$$\Omega_c(z, t) = \Omega(z, t) \cos[\varphi(z, t)], \quad (3)$$

$$\Omega_s(z, t) = -\Omega(z, t) \sin[\varphi(z, t)]. \quad (4)$$

Based on these two field components, the Bloch equations in the rotating frame [15] can be rewritten as

$$\frac{dr_1(z, t, \Delta)}{dt} = \Delta r_2(z, t, \Delta) + r_3(z, t, \Delta) \Omega_s(z, t) - \frac{r_1(z, t, \Delta)}{T_2}, \quad (5)$$

$$\frac{dr_2(z, t, \Delta)}{dt} = -\Delta r_1(z, t, \Delta) + r_3(z, t, \Delta) \Omega_c(z, t) - \frac{r_2(z, t, \Delta)}{T_2}, \quad (6)$$

$$\frac{dr_3(z, t, \Delta)}{dt} = -r_2(z, t, \Delta) \Omega_c(z, t) - r_1(z, t, \Delta) \Omega_s(z, t) - \frac{1 + r_3(z, t, \Delta)}{T_1} \quad (7)$$

where $r_1(z, t, \Delta)$ and $r_2(z, t, \Delta)$ are the in-phase and in-quadrature components of the atoms' polarization, respectively, $r_3(z, t, \Delta)$, the population inversion, and T_2 denotes the coherence dephasing time. The lifetime T_1 of the excited state is usually neglected by assuming an input pulse sequence much shorter than T_1 , unless the accumulated stimulated photon echo process is investigated. The frequency detuning $\Delta = \omega - \omega_0$ is the difference between the atom's resonant frequency ω and the laser frequency ω_0 . The polarization obtained from the Bloch equations is

$$\tilde{P}(z, t) = P_c(z, t) \cos(\omega t - kz) + P_s(z, t) \sin(\omega t - kz), \quad (8)$$

where

$$P_c(z, t) = N\mu \int_{-\infty}^{\infty} r_1(z, t, \Delta) g(\Delta) d\Delta, \quad (9)$$

$$P_s(z, t) = -N\mu \int_{-\infty}^{\infty} r_2(z, t, \Delta) g(\Delta) d\Delta, \quad (10)$$

where $g(\Delta)$ represents the inhomogeneous line shape, and N is the atom density. The propagation equations of the two-field components are

$$\frac{\partial \Omega_c(z, t)}{\partial z} + \frac{n}{c} \frac{\partial \Omega_c(z, t)}{\partial t} = \frac{\omega_0}{2\varepsilon_0 c} P_s(z, t), \quad (11)$$

$$\frac{\partial \Omega_s(z, t)}{\partial z} + \frac{n}{c} \frac{\partial \Omega_s(z, t)}{\partial t} = -\frac{\omega_0}{2\varepsilon_0 c} P_c(z, t), \quad (12)$$

where n is the index of refraction. Using the retarded time by replacing t with $t - z/c$ and combining Eqs. (9)–(12), the field propagation equations are obtained as

$$\frac{d\Omega_c(z, t')}{dz} = \frac{\alpha}{2\pi} \int_{-\infty}^{\infty} r_2(z, t', \Delta) g(\Delta) d\Delta, \quad (13)$$

$$\frac{d\Omega_s(z, t')}{dz} = -\frac{\alpha}{2\pi} \int_{-\infty}^{\infty} r_1(z, t', \Delta) g(\Delta) d\Delta, \quad (14)$$

where α is the intensity absorption coefficient at the center frequency. Eqs. (5)–(7), (13) and (14) comprise the coupled Maxwell–Bloch equations. The problem can be solved by a well-established procedure that divides the medium into thin layers along the direction z . Bloch equations (5)–(7) are solved for each layer, using the field incident onto that layer. Propagation equations (13) and (14) calculate the contribution of the polarization of the medium to the propagating field, which will be the input for the next layer.

2.2. Angled beam Maxwell–Bloch equations

The model can be modified to handle multiple beam propagation, such as the box configuration discussed in Fig. 1(a). To keep the discussion simple, we first deal with the fields propagating along two directions symmetric to the

z -axis, $\vec{k}_+ = \vec{k}_z + \vec{k}_x$ and $\vec{k}_- = \vec{k}_z - \vec{k}_x$, as shown in Fig. 1(b), where the field can be written as

$$E(x, z, t) = \frac{\hbar}{\mu} \left[\Omega^+(z, t) \cos(\omega_0 t - k_z z - k_x x) + \Omega^-(z, t) \cos(\omega_0 t - k_z z + k_x x) \right], \quad (15)$$

where k_z and k_x are the wave vector components along z and x axes, respectively. $\Omega^+(z, t)$ and $\Omega^-(z, t)$ are the Rabi frequencies of input fields propagating along k_+ and k_- , respectively. The fields are only functions of z and t , and the propagation effects along x -axis are treated as spatial phase modulation ($k_x x$). The field expression (15) becomes

$$E(x, z, t) = \frac{\hbar}{\mu} \left[\Omega_c(x, z, t) \cos(\omega_0 t - k_z z) + \Omega_s(x, z, t) \sin(\omega_0 t - k_z z) \right], \quad (16)$$

where

$$\Omega_c(x, z, t) = [\Omega^+(z, t) + \Omega^-(z, t)] \cos(k_x x), \quad (17)$$

$$\Omega_s(x, z, t) = [-\Omega^+(z, t) + \Omega^-(z, t)] \sin(k_x x). \quad (18)$$

These field components vary along the transverse axis, due to the spatial phases associated with the propagation direction. Therefore, the Bloch components of the atoms also become functions of x . The Bloch equations become

$$\frac{dr_1(x, z, t, \Delta)}{dt} = \Delta r_2(x, z, t, \Delta) + r_3(x, z, t, \Delta) \Omega_s(x, z, t) - \frac{r_1(x, z, t, \Delta)}{T_2}, \quad (19)$$

$$\frac{dr_2(x, z, t, \Delta)}{dt} = -\Delta r_1(x, z, t, \Delta) + r_3(x, z, t, \Delta) \Omega_s(x, z, t) - \frac{r_2(x, z, t, \Delta)}{T_2}, \quad (20)$$

$$\frac{dr_3(x, z, t, \Delta)}{dt} = -r_2(x, z, t, \Delta) \Omega_c(x, z, t) - r_1(x, z, t, \Delta) \Omega_s(x, z, t) - \frac{1 + r_3(x, z, t, \Delta)}{T_1}. \quad (21)$$

Applying Eqs. (17) and (18) to Eqs. (13) and (14), the propagation equations become

$$\left(\frac{d[\Omega^-(z, t') + \Omega^+(z, t')]}{dz} \right) \cos(k_x x) = \frac{\alpha}{2\pi} \int_{-\infty}^{\infty} r_2(x, z, t', \Delta) g(\Delta) d\Delta, \quad (22)$$

$$\left(\frac{d[\Omega^-(z, t') - \Omega^+(z, t')]}{dz} \right) \sin(k_x x) = -\frac{\alpha}{2\pi} \int_{-\infty}^{\infty} r_1(x, z, t', \Delta) g(\Delta) d\Delta. \quad (23)$$

From the above equations, the propagation equation of the fields along the two beams can be obtained as

$$\frac{d\Omega^+(z, t')}{dz} = \frac{\alpha}{4\pi^2} \int_0^{2\pi} \int_{-\infty}^{\infty} [r_2(x, z, t', \Delta) \cos(k_x x) + r_1(x, z, t', \Delta) \sin(k_x x)] g(\Delta) d\Delta d(k_x x), \quad (24)$$

$$\frac{d\Omega^-(z, t')}{dz} = \frac{\alpha}{4\pi^2} \int_0^{2\pi} \int_{-\infty}^{\infty} [r_2(x, z, t', \Delta) \cos(k_x x) - r_1(x, z, t', \Delta) \sin(k_x x)] g(\Delta) d\Delta d(k_x x). \quad (25)$$

These two equations only track the field along the two specified directions \vec{k}_+ and \vec{k}_- . In most experimental settings, the input directions and timings are arranged so that the echo carrying desired signals comes out along one of these two directions. However, higher order echoes ($m > 1$) in this setting may propagate in directions, $\vec{k}_e^m = \vec{k}_3 + m(\vec{k}_2 - \vec{k}_1)$. Therefore, a general numerical model for any direction is required to evaluate higher order echoes, and for the cases of multiple inputs incident in multiple directions.

2.3. Maxwell–Bloch equations for multiple angled beams

The box geometry shown in Fig. 1(b) is an example of a multiple angled beam configuration, which has been used for many OCT processes. For beams incident along an arbitrary direction, k has components in transverse directions x , y , and

propagation direction z , which still can be defined under small-angle assumption. The multiple-beam field can be written as

$$E(\vec{R}, z, t) = \frac{\hbar}{\mu} \sum_{k_{xy}>0} [\Omega^{+k_{xy}}(z, t) \cos(\omega_0 t - k_z z - \vec{k}_{xy} \cdot \vec{R}) + \Omega^{-k_{xy}}(z, t) \cos(\omega_0 t - k_z z + \vec{k}_{xy} \cdot \vec{R})], \quad (26)$$

where \vec{k}_{xy} is a transverse wave vector corresponding to the direction in the xy -plane and it is assumed that $\vec{k}_{xy} \neq 0$, \vec{R} is the spatial vector in the xy -plane. This field can still be written in the form as Eq. (16):

$$E(\vec{R}, z, t) = \frac{\hbar}{\mu} [\Omega_c(\vec{R}, z, t) \cos(\omega_0 t - k_z z) + \Omega_s(\vec{R}, z, t) \sin(\omega_0 t - k_z z)], \quad (27)$$

where

$$\Omega_c(\vec{R}, z, t) = \sum_{k_{xy}>0} [(\Omega^{+k_{xy}}(z, t) + \Omega^{-k_{xy}}(z, t)) \cos(\vec{k}_{xy} \cdot \vec{R})], \quad (28)$$

$$\Omega_s(\vec{R}, z, t) = \sum_{k_{xy}>0} [(-\Omega^{+k_{xy}}(z, t) + \Omega^{-k_{xy}}(z, t)) \sin(\vec{k}_{xy} \cdot \vec{R})]. \quad (29)$$

The generated polarizations act as a source to the field. In the layer at z in the medium, the polarization is a function of \vec{R} , given as

$$\tilde{P}(\vec{R}, z, t) = P(\vec{R}, z, t) \cos(\omega_0 t - k_z z - \vec{k}_{xy} \cdot \vec{R}) \quad (30)$$

that can be expressed as in-phase and out-of-phase components

$$\tilde{P}(\vec{R}, z, t) = P_c(\vec{R}, z, t) \cos(\omega_0 t - k_z z) + P_s(\vec{R}, z, t) \sin(\omega_0 t - k_z z), \quad (31)$$

where

$$P_c(\vec{R}, z, t) = P(\vec{R}, z, t) \cos(\vec{k}_{xy} \cdot \vec{R}), \quad (32)$$

$$P_s(\vec{R}, z, t) = P(\vec{R}, z, t) \sin(\vec{k}_{xy} \cdot \vec{R}). \quad (33)$$

Under the condition that the angles are small, $P(\vec{R}, z, t)$ can be obtained from the collinear calculation at the spatial point (R, z) , where x in Bloch equations (19)–(21) is replaced by \vec{R} and k_x is replaced by \vec{k}_{xy} . The propagation equations will

become

$$\sum_{\vec{k}_{xy}} \left[\frac{d[\Omega^{-k_{xy}}(z, t') + \Omega^{+k_{xy}}(z, t')]}{dz} \cos(\vec{k}_{xy} \cdot \vec{R}) \right] = \frac{\alpha}{2\pi} \int_{-\infty}^{\infty} r_2(\vec{R}, z, t', \Delta) g(\Delta) d\Delta, \quad (34)$$

$$\sum_{\vec{k}_{xy}} \left[\frac{d[\Omega^{-k_{xy}}(z, t') - \Omega^{+k_{xy}}(z, t')]}{dz} \sin(\vec{k}_{xy} \cdot \vec{R}) \right] = -\frac{\alpha}{2\pi} \int_{-\infty}^{\infty} r_1(\vec{R}, z, t', \Delta) g(\Delta) d\Delta. \quad (35)$$

The propagation for any beam can be obtained using Fourier transform

$$\frac{d\Omega^{+k_{xy}}(z, t')}{dz} = \frac{\alpha}{8\pi^3} \int_0^{2\pi} \int_0^{2\pi} \int_{-\infty}^{\infty} [r_2(\vec{R}, z, t', \Delta) \cos(\vec{k}_{xy} \cdot \vec{R})x + r_1(\vec{R}, z, t', \Delta) \sin(\vec{k}_{xy} \cdot \vec{R})] \times g(\Delta) d\Delta d(k_x)x d(k_y)y, \quad (36)$$

where $\vec{k}_{xy} \cdot \vec{R} = k_x x + k_y y$ is applied. Similarly, $d\Omega^{-k_{xy}}(z, t')/dz$ can be obtained by changing the sign of \vec{k}_{xy} in Eq. (36).

2.4. Numerical solution of the Maxwell–Bloch equations with angled beam

The numerical procedure will be discussed under two assumptions. First, the fields are plane waves propagating forward. Second, the angles between the beams are small so that the angled beam configuration only results in the spatial phase variation in the direction transverse to the main propagation direction. Applications of the spatial phase-matching condition to the propagating beams is needed before doing the numerical solution in order to decide which beams should be included in the calculation.

To solve the Maxwell–Bloch equations numerically, two sets of grids are defined to carry out the integrations: one for the field components and the other for the Bloch components. The grid for the fields is two-dimensional and consists of the propagation axis z and the time axis t . At each location on the z – t grid, two extra dimensions,

x and Δ , are added to solve Bloch equations (19)–(21). The initial conditions of the Bloch components at $t = 0$ are usually set to $r_1 = 0$, $r_2 = 0$, $r_3 = -1$, which means all atoms at their ground states. After the Bloch equations driven by the incident field are solved, the Bloch components on their four-dimensional grid are updated. At each z location, the field components are calculated along the t -axis using the integrations of the propagation Eq. (36) by bringing the Bloch components into the right-hand side of the equation. Then, the calculation moves forwards to the next point on the z -grid using the fields obtained at the previous location as the input.

The length of the z -dimension is the thickness of the medium. The number of steps in this dimension should satisfy the condition $\alpha dz < 0.05$. A minimum number of time points in the pulse sequences is required so that there are enough points in the shortest pulse to avoid the analogue signal distortion. In the frequency domain, the minimum number of steps depends on the finest spectral structure and the time length of the pulse sequences. In the simulations, the integration range is usually chosen to be several times greater than the range of the spectral grating. It is sufficient to define the transverse spatial phase $k_{x,x}$ as one variable instead of the individual wave vector. For the spatial Fourier transform in Eq. (36), the integration over $k_{x,x}$ is calculated only for one period. The number of steps in this dimension should be set sufficiently high to separate the beams of interest. This number is much smaller than that which would be required to calculate the full field distribution in the transverse dimensions.

3. Simulations using Maxwell–Bloch equations for angled beam

3.1. OCT correlator

OCT techniques have been used to perform correlations of three temporally modulated light pulses for RF signal processing [2,17]. Fig. 1(b) shows a typical input beam arrangement, where three pulses with amplitudes of $E_1(t)$, $E_2(t)$ and

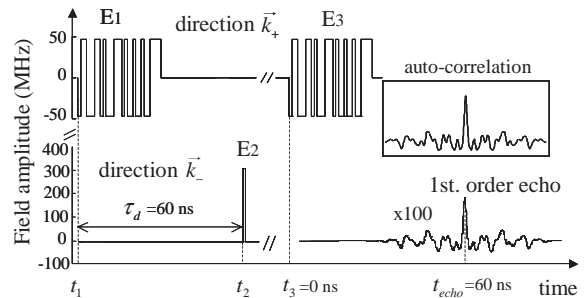


Fig. 2. Simulation of optical correlators. Thirty-bit bi-phase pattern A at 1 GHz/bit rate is carried by the programming pulse $E_1(t)$ and the probe pulse $E_3(t)$ in direction \vec{k}_+ , plotted in the top trace. The 1-ns-long brief reference pulse $E_2(t)$ in direction \vec{k}_- and the resulting first-order echo are plotted in the lower trace. The inset is the auto-correlation function of pattern A calculated using Fourier transform. The field amplitude is in terms of Rabi frequency.

$E_3(t)$, respectively, are sent into the medium consecutively at times, t_1 , t_2 and t_3 , respectively (as shown in Fig. 2), with pulses 1 and 3 in direction \vec{k}_+ , and pulse 2 in direction \vec{k}_- . The time interval between the second and the third pulse is longer than the coherence time of the medium T_2 . This input sequence produces the first order stimulated echo, in direction \vec{k}_- , with the temporal profile which is the correlation of $E_1(t)$ with the convolution of $E_2(t)$ and $E_3(t)$. The echo is delayed from pulse 3 by the time interval, τ_d , the delay between the first two pulses. In Fig. 2, we simulate the first-order echo for two-beam geometry by choosing $E_1(t)$ and $E_3(t)$ (called programming and probe, respectively) from a set of 30-bit binary phase-modulated patterns at 1 Gbit/s and $E_2(t)$, a 1 ns brief pulse (called reference). The shape of the first order of stimulated echo is expected to be the correlation between the patterns carried by pulses 1 and 3: auto-correlation when the same patterns on both pulses and cross-correlation when they are different patterns. The top trace represents the programming and the probe pulses carrying the same pattern A, with a pulse area of 0.015π on each bit. The lower trace shows the brief reference pulse with a pulse area of 0.1π and the first-order echo field generated from the medium. The inset gives the autocorrelation function of the pattern, as calculated using Fourier transform. It is clear that the first-order echo takes the shape of the

auto-correlation of the pattern. In this setup, the advantage of the two-beam geometry is to pull out the first-order echo from other signals, such as the inputs, the free induction decay and the higher order echoes, which may be temporally overlapped with the desired echo signal. This is especially important for the situation where the probe field is continuous, as shown in Fig. 3. The beam setup is the same as that in Fig. 2, except that the probe pulse carries a long pattern consisting of many 30-bit patterns including pattern A. The echo is temporarily overlapped with the probe pulse, but in a different direction, so that the echo can be detected separately. The top trace in Fig. 3 shows the input of a 180-bit segment of a continuous probe and the resulting echo is plotted in the lower trace. There are two patterns in the probe that are identical to the programming pattern A and four randomly chosen 30-bit patterns (*W*, *X*, *Y*, and *Z*). The simulation shows two peaks in the echo signal, indicating that two parts in the probe pattern are identical or very close to the programming pattern.

The idea of the OCT analog correlator is to utilize the temporal property of the first-order echo. However, some undesired effects arise in the process, such as the saturation during the programming and/or probe causing the distortion of the pattern and the cross-talks between the

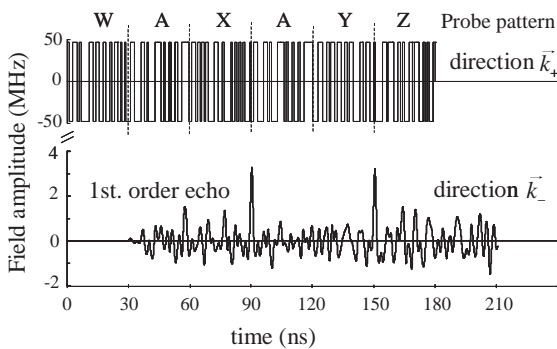


Fig. 3. Simulation of the echo from a continuous probe. The programming and the reference pulses are the same as those in Fig. 2. The probe is a 180-bit long pattern, including two segments identical to pattern A and four random patterns, *W*, *X*, *Y*, and *Z* (in top trace). The echo plot in the lower trace shows two peaks, indicating the two segments match the programming pattern.

patterns. Simulation of the processes including the higher-order echoes provide the information necessary to define the operation conditions and the dynamic range. We simulated the process of continuous programming based on the accumulated SPE process [15,16]. The settings are similar to those used for Fig. 2, the pair of programming pulses and the reference pulse have the same timing and the same directions except it was repeated one more time before the probe pulse was sent into the medium. The accumulation process results in high echo efficiency with low programming power and the dynamical change of the patterns on the fly. However, the higher order echoes are inherent in the process. In Fig. 4, we simulated this process by tracking four beams: \vec{k}_{\pm} and $\vec{k}_{\pm 3} = \vec{k}_z \pm 3\vec{k}_x$. The input probe field used in the simulation is plotted in the top trace, the resulting first echo in the middle trace, and the second-order echo in the bottom trace. The first-order echo propagating along \vec{k}_{-} takes the shape of the auto-correlation of pattern A at about twice the amplitude as in Fig. 2. The echo efficiency increases due to the accumulation. The

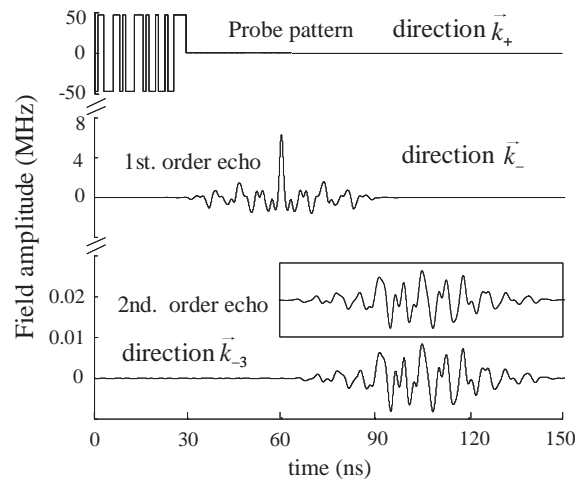


Fig. 4. Simulation of accumulated process. The programming and reference pair are the same as in Fig. 2, but are applied twice with time interval between the shots longer than the medium coherence time. The top trace shows the same probe as in Fig. 2. The first-order echo (the middle trace) is in direction \vec{k}_{-} and the second-order echo (the bottom trace) in direction $\vec{k}_{-3} = \vec{k}_z - 3\vec{k}_x$. The inset is the predicted shape of the second-order echo calculated with Fourier transform.

second-order echo is expected to have the shape of the convolution between pattern A and its auto-correlation function. The expected function is plotted in the inset, to which the echo field matches well. The second-order echo has a wave vector $\vec{k}_{-3} = \vec{k}_z - 3\vec{k}_x$. Whether or not this second-order echo propagates along that direction in an experiment is determined by the spatial phase-matching condition.

3.2. Simulation for quasi-continuous probe

In some of the OCT processors, such as the optical coherent transient true-time delay and optical analog correlator, it is required that the probe pulse in the three-pulse input of the photon echo process be temporally long or continuous. Although the long probe pulses are amplitude or phase modulated in some settings, which reduces the saturation at certain frequencies, the output data suffer the deterioration from the saturation effects from the probe pulse when the probe time eventually exceeds certain limits. To study the echo's temporal behavior with a long probe field, a photon echo process with two brief programming pulses followed by a long square probe pulse is a simple case. In this section, we present the simulation to explore the temporal and spatial behaviors of the SPEs generated in this process and the optical nutation on the transmitted probe fields. As described above in Fig. 1(b), the temporally overlapped probe and echo pulses are spatially separated with an angled beam configuration, two brief programming pulses propagate along \vec{k}_+ and \vec{k}_- , respectively. In a normal-angled beam SPE process as shown in Fig. 5(a), a probe along direction \vec{k}_+ results in an echo in the direction \vec{k}_- according to the rule of the causality [18,19] (we call it the causal direction). Fig. 5(b) illustrates an unusual spatial arrangement with a probe incident along \vec{k}_- . As well known, if the probe is a brief pulse, no echo is generated in direction \vec{k}_+ because of causality. However, the situation for a long probe is completely different. The two traces from the top of Fig. 6 show that echoes are generated in both the causal and non-causal directions. In the simulation, we set the pulse area of the two brief pulses to $\pi/2$ and the 10-

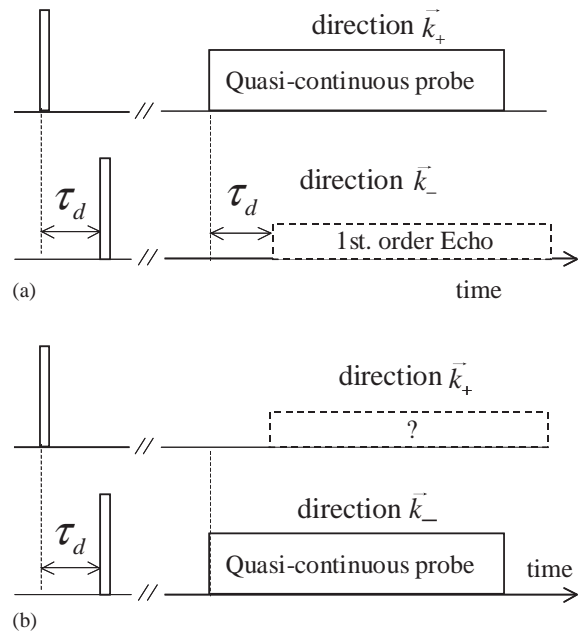


Fig. 5. The schematic of angled beam setup for two brief pulses followed by a quasi-continuous probe. The first and the second brief pulses were along \vec{k}_+ and \vec{k}_- , respectively. (a) When the probe was along \vec{k}_+ , an echo is generated along \vec{k}_- (called the causal direction). (b) When the probe is along \vec{k}_- , an echo generated is along \vec{k}_+ (called the no-causal direction).

μs -long probe to 18π . In the two traces, the delay was $0.15\ \mu\text{s}$ (top) and $0.3\ \mu\text{s}$ (middle), respectively, which is the same as those in Fig. 3 of Ref. [12]. When the probe is longer than the delay and the probe pulse area is larger than the saturation level, π , the transmitted probe shows the behavior of a normal optical nutation (the bottom trace), which is independent of the probe direction and the delay. The echoes also have a nutation-like oscillatory profile, which makes the echoes distorted from the input probe of uniform amplitude. This distortion comes from the saturation effect caused by the long probe. The echoes in the non-causal direction \vec{k}_+ have the same delay and a similar oscillation as the first-order echoes in the causal direction, yet from a different coherent transient process. The front part of the long probe generates a coherence in direction $2\vec{k}_- - \vec{k}_+$ at time $t_3 + \tau_d$, whose propagation as a field may be forbidden according to the spatial phase-matching requirement; however, a later part of the probe

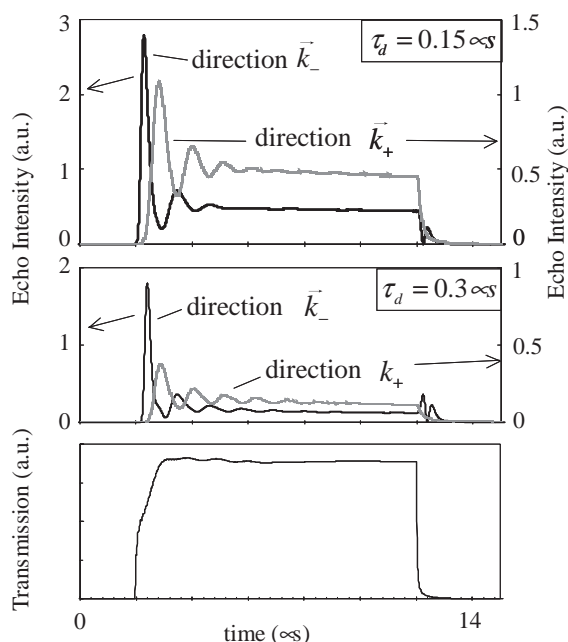


Fig. 6. The simulation results of echoes generated by two brief pulses and a 10 μ s-long probe in both the causal (\vec{k}_-) and non-causal (\vec{k}_+) directions. The arrows indicate the different vertical scales for the echoes in different directions. The top two traces show the echoes for different delays, as indicated in the graphs. All the other parameters are the same for both cases. The bottom trace gives the optical nutation on the transmitted probe pulse, which does not change with the probe direction and the delay.

rephases this coherence, through a two-pulse echo process, into an echo propagating in the allowed direction \vec{k}_+ . In order to see this echo, the probe duration has to be longer than the delay. These simulation results match the experiment described in Ref. [12].

4. Conclusion

We have developed a theoretical model based on Maxwell–Bloch equations for angled beams geometry. Under some realistic assumptions, namely, small-angle and reflection-free propagation, we have replaced the calculation of the three-dimensional spatial distribution of the fields by tracking fields in a few preset directions using spatial Fourier transform. This radical change made the simulations for most of

the geometrical settings of optical coherent transient processes feasible within a reasonable computing time. We have developed the numerical simulator and perform the simulations with two and four beams. The simulation results matched the predictions and the experiments very well.

Acknowledgements

We wish to thank K.D. Merkel and R.K. Mohan for the discussions on the simulations of the optical correlator. The authors would like to acknowledge the support from an AFOSR grant (F49620-98-1-0283) and a DEPCoR grant (F49620-02-1-0275).

References

- [1] T.W. Mossberg, *Opt. Lett.* 7 (1982) 77.
- [2] W.R. Babbitt, J.A. Bell, *Appl. Opt.* 33 (1994) 1538.
- [3] W.R. Babbitt, T.W. Mossberg, *Opt. Lett.* 20 (1995) 910.
- [4] K.D. Merkel, W.R. Babbitt, *Opt. Lett.* 21 (1996) 1102.
- [5] Z.W. Barber, M. Tian, R.R. Reibel, W.R. Babbitt, *Opt. Exp.* 10 (2002) 1145.
- [6] C. Greiner, B. Boggs, T. Loftus, T. Wang, T.W. Mossberg, *Phys. Rev. A* 60 (1999) R2657.
- [7] T. Wang, C. Greiner, J.R. Bochinski, T.W. Mossberg, *Phys. Rev. A* 60 (1999) R757.
- [8] T. Wang, C. Greiner, T.W. Mossberg, *Opt. Commun.* 153 (1998) 309.
- [9] R.W. Olson, H.W.H. Lee, F.G. Patterson, M.D. Fayer, *J. Chem. Phys.* 76 (1982) 31.
- [10] M. Azadeh, C. Sjaarda Cornish, W.R. Babbitt, L. Tsang, *Phys. Rev. A* 57 (1998) 4662.
- [11] L. Menager, I. Lorgere, J-L. LeGouet, D. Dolfi, J-P. Huignard, *Opt. Lett.* 26 (2001) 1245.
- [12] M. Tian, R. Reibel, Z. Barber, W.R. Babbitt, *Opt. Lett.* 27 (2002) 1156.
- [13] M.O. Scully, M.S. Zubairy, *Quantum Optics*, Cambridge University, Cambridge, 1997.
- [14] J.I. Steinfeld, *Laser and Coherence Spectrum*, Plenum Press, New York, 1978.
- [15] L. Mandel, E. Wolf, *Optical Coherences and Quantum Optics*, Cambridge University, Cambridge, 1995.
- [16] K.D. Merkel, R.D. Peters, P.B. Sellin, K.S. Repasky, W.R. Babbitt, *Opt. Lett.* 25 (2000) 1627.
- [17] M. Tian, J. Zhao, Z. Cole, R. Reibel, W.R. Babbitt, *J. Opt. Soc. Am. B* 18 (2001) 673.
- [18] S. Bernet, B. Kohler, A. Rebane, A. Renn, Urs.P. Wild, *J. Opt. Soc. Am. B* 9 (1992) 987.
- [19] A. Rebane, S. Bernet, A. Renn, .Wild Urs P, *Opt. Commun.* 86 (1991) 7.